

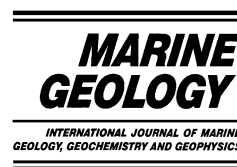


ELSEVIER

Available online at [www.sciencedirect.com](http://www.sciencedirect.com)

SCIENCE @ DIRECT®

Marine Geology 205 (2004) 227–247



[www.elsevier.com/locate/margeo](http://www.elsevier.com/locate/margeo)

# Chronostratigraphy of ODP 181, Site 1121 sediment core (Southwest Pacific Ocean), using $^{10}\text{Be}/^9\text{Be}$ dating of entrapped ferromanganese nodules

I.J. Graham<sup>a,\*</sup>, R.M. Carter<sup>b</sup>, R.G. Ditchburn<sup>a</sup>, A. Zondervan<sup>a</sup>

<sup>a</sup> *Institute of Geological and Nuclear Sciences Ltd. (GNS), P.O.Box 31-312, Lower Hutt, New Zealand*

<sup>b</sup> *Marine Geophysical Laboratory, James Cook University, Townsville, Qld 4811, Australia*

Received 15 August 2002; received in revised form 14 July 2003; accepted 14 July 2003

## Abstract

A  $^{10}\text{Be}/^9\text{Be}$ -based chronostratigraphy has been determined for ODP 181, Site 1121 sediment core, recovered from the foot of the Campbell Plateau, Southwest Pacific Ocean. This core was drilled through the Campbell 'skin drift' in ca. 4500 m water depth on the mid-western margin of the extensive Campbell Nodule Field, beneath the flow of the major cold-water Deep Western Boundary Current (DWBC). In the absence of detailed biostratigraphy, beryllium isotopes have provided essential time information to allow palaeo-environmental interpretation to be undertaken on the upper 7 m of the core. Measured  $^{10}\text{Be}/^9\text{Be}$  ratios of sediment, and of ferromanganese nodules entrapped in the sediment, decrease systematically with depth in the core, in accordance with radioactive decay. However, the  $^{10}\text{Be}/^9\text{Be}$  data diverge from ca. 3 m below the seafloor (mbsf) to the top of the core, giving rise to several possible geochronological models. The preferred model assumes that the measured  $^{10}\text{Be}/^9\text{Be}$  ratios of the nodule rims reflect initial  $^{10}\text{Be}/^9\text{Be}$  ratios equivalent to contemporary seawater, and that these can be used to derive the true age of the sediment where the nodules occur. The nodule rim ages can be then used to interpret the sediment  $^{10}\text{Be}/^9\text{Be}$  data, which indicate an overall age to ca. 7 mbsf of ca. 17.5 Ma. The derived chronology is consistent with diatom biostratigraphy, which indicates an age of 2.2–3.6 Ma at 1 mbsf. Calculated sedimentation rates range from 8 to 95 cm m.y.<sup>-1</sup>, with an overall rate to 7 mbsf of ca. 39 cm m.y.<sup>-1</sup>. The lowest rates generally coincide with the occurrence of entrapped nodules, and reflect periods of increased bottom current flow causing net sediment loss. Growth rates of individual nodules decrease towards the top of the sediment core, similar to the observed decrease in growth rate from core to rim of seafloor nodules from the Campbell Nodule Field. This may be related to an overall increase in the vigour of the DWBC from ca. 10 Ma to the present.

© 2004 Elsevier B.V. All rights reserved.

**Keywords:** Campbell Plateau; ODP 181 Site 1121; ferromanganese nodules; deep-sea sediments;  $^{10}\text{Be}$  dating

## 1. Introduction

Site 1121 was drilled during ODP Leg 181 in 4503 m water depth at the eastern foot of the Campbell Plateau, Southwest Pacific Ocean (Fig.

\* Corresponding author. Tel.: +64-4-5704-677;  
Fax: +64-4-5704-657.

E-mail address: [i.graham@gns.cri.nz](mailto:i.graham@gns.cri.nz) (I.J. Graham).

1). The site is located at the western edge of the Campbell Nodule Field (Wright et al., 2003), beneath the path of the cold-water Deep Western Boundary Current (DWBC) and the Antarctic Circumpolar Current (ACC) (Carter and McCave, 1997). At that location, the sediment core has the potential to provide key palaeo-environmental and palaeo-ecological information on an important segment of the New Zealand continental margin (i.e. the Campbell 'skin drift'). Previous attempts to obtain a drill core in the vicinity of Site 1121 (i.e. DSDP Sites 275 and 276; Fig. 1) were unsuccessful, with only 17.5 m of core (41% recovery) obtained from DSDP 275

and none from DSDP 276, after hard surficial layers were encountered (Kennett et al., 1973).

The top-most 15.2 m of the Site 1121 core, Unit 1A, comprises alternating beds of slightly bioturbated yellow-brown and grey-brown silty-sandy clay and sandy-clayey silt. Malvern particle size analysis to 7.42 mbsf indicates that the sediment is generally fine-grained (33–83  $\mu\text{m}$  mean diameter), and consists of four well-sorted modal grain-sizes (Table 1) whose relative proportions vary towards the top of the core: (1) from 7.42 to 5.90 mbsf, fine sandy-clayey silt dominates; (2) from 5.26 to 4.16 mbsf, clayey-sandy silt dominates; (3) from 3.86 to 0.16 mbsf, coarse silt dom-

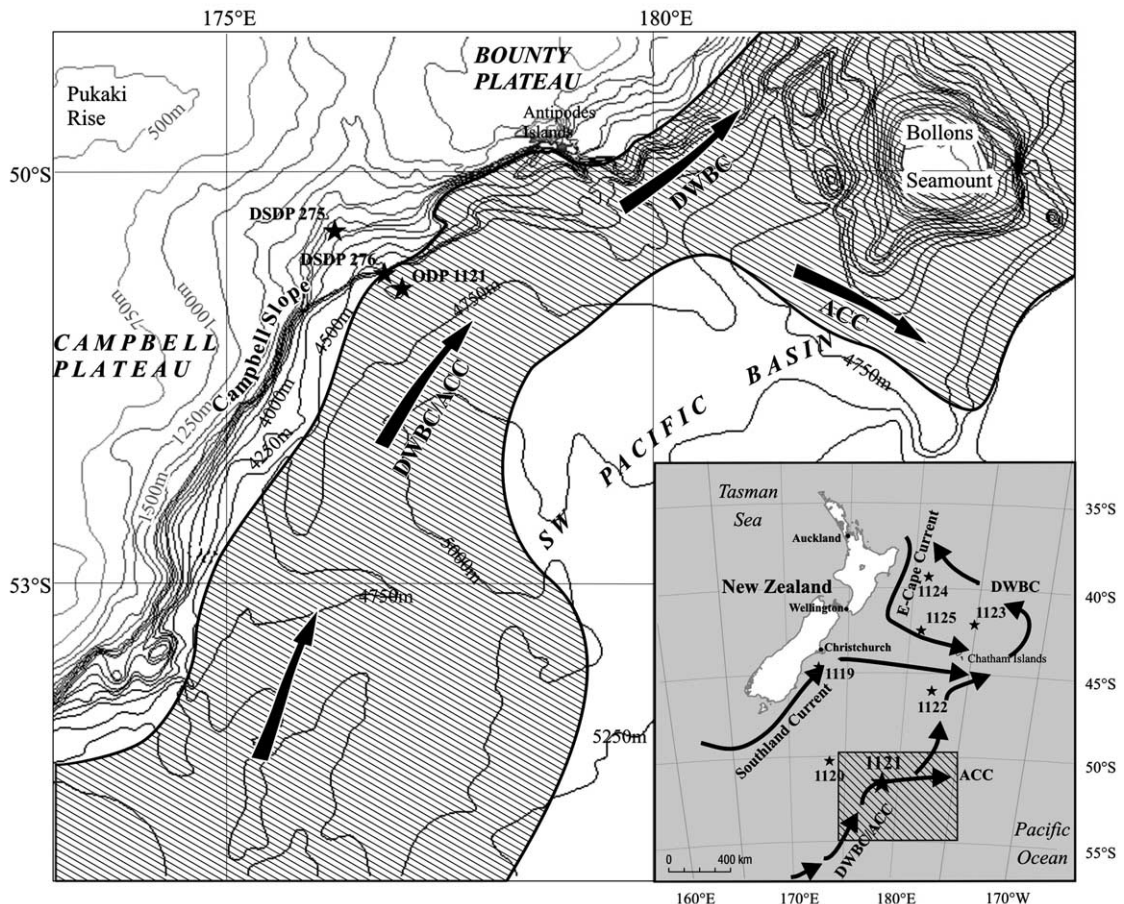


Fig. 1. Bathymetric map of the Southwest Pacific Ocean, showing the location of DSDP Sites 275–276, ODP 181 Sites 1119–1125 and oceanic currents. Cross-hatching indicates the present distribution of the Campbell Nodule Field. Abbreviations: DWBC, Deep Western Boundary Current; ACC, Antarctic Circumpolar Current.

inates, and the mean grain-size decreases to a minimum at 2.35 mbsf, then gradually increases to a maximum at the top of the core. This indicates generally quiet, clay-rich conditions below ca. 4 mbsf, with increasingly more vigorous, silty–sandy conditions above. The upper ca. 4 m of the core contains occasional ferromanganese nodules, and is probably palimpsest throughout.

Despite an abundance of microfossils and nanofossils, the biostratigraphy of Unit IA is poorly delineated (Carter et al., 1999). Benthic foraminifera indicate a Palaeocene age (> 55 Ma) below ca. 29 mbsf, but diatoms provide the most useful age information for the upper part:

mbsf	Ma
0.00–0.36	0.0–0.4
0.36–0.90	0.7–1.8
1.00–1.02	2.2–3.6
1.02–1.03	3.3–3.6

This, however, indicates only that the Site 1121 sediment core represents a condensed sequence of Plio–Pleistocene age, underlain by unspecified late Neogene deposits. A more soundly based and detailed chronostratigraphy is essential to fully reveal the palaeo-environmental history contained in the core. The absence of detailed biostratigraphic information or suitable materials for standard radiometric dating (e.g. Ar–Ar analysis of intercalated volcanic materials) has, therefore, prompted us to apply a comparatively new and largely untested  $^{10}\text{Be}$  dating methodology to the upper ca. 15 m of the core, with some success. We report here  $^{10}\text{Be}$  analytical results for sediment and entrapped ferromanganese nodules (Sections 2 and 3), discuss geochronological interpretations of these data (Sections 4 and 5) and, on the basis of a preferred age model, make some broad inferences regarding past activity of the DWBC (Section 6).

## 2. Dating methodology

The cosmogenic isotope  $^{10}\text{Be}$  is produced mainly in the upper atmosphere via spallation of

oxygen and nitrogen nuclei by cosmic ray neutrons. Shortly after formation,  $^{10}\text{Be}$  is adsorbed onto aerosols and removed from the atmosphere by precipitation, then enters the oceans by fluvial and/or aeolian transport where it becomes incorporated in a variety of oceanic deposits (McHargue and Damon, 1991). Ferromanganese nodules grow by accretion from seawater either just above the abyssal seafloor (i.e. hydrogenous growth) or just below the seafloor (i.e. diagenetic growth), and absorb  $^{10}\text{Be}$  during their growth from which their ages can be determined (e.g. Mangini et al., 1990; von Stackelberg, 1997; von Blanckenburg and O’Nions, 1999).

The  $^{10}\text{Be}$  dating method as it applies to ferromanganese nodules is based on the relative isotopic composition (i.e. decay difference) between growth layers (see Baturin and Savenko, 1989; Somayajulu, 2000):

$$\text{Age Difference} = (t_{1/2}/\ln(2)) \ln(I/O) \quad (1)$$

where the radiometric half-life  $t_{1/2} = 1.5 \pm 0.1$  m.y. (Bhat et al., 1973)<sup>1</sup>, and  $I$  and  $O$  are the measured isotopic concentrations of the inner and outer layers, respectively. This equation, which is independent of the concentration of the daughter isotope  $^{10}\text{B}$ , holds true only if both layers had the same initial isotopic concentrations at the time of formation, and post-formational isotopic exchange is minimal.

Here, we have chosen to apply the isotopic ratio  $^{10}\text{Be}/^9\text{Be}$ , rather than the  $^{10}\text{Be}$  concentration, to Eq. 1 since the former parameter, at the growth surface of a nodule, is expected to have been less variant through time (see Segl et al., 1984, 1989). The overall chemical composition of ferromanganese nodules is known to vary considerably during growth due to changes in seawater chemistry, pH, temperature etc. (Kusakabe and Ku, 1984; Mangini et al., 1986, 1990), so it is to be expected

<sup>1</sup> Recent reanalysis by Nishiizumi (2002) of the NIST standard (see Middleton et al., 1993) has suggested that this value may be too high by ca. 15%. If so, then all  $^{10}\text{Be}$  atoms  $\text{g}^{-1}$  values quoted here will be 15% high. However, such an adjustment does not affect  $^{10}\text{Be}$  concentration ratios and, therefore, calculated ages will remain invariant under future corrections to the NIST standard.

Table 1  
Malvern particle size data for sediments from the upper part of Site 1121 sediment core

Sample field number	Depth in core (mbfs)	Mean grain-size ( $\mu\text{m}$ )	Clay (%)	Silt (%)	Sand (%)	Mode I ( $\mu\text{m}$ )	Mode II ( $\mu\text{m}$ )	Mode III ( $\mu\text{m}$ )	Mode IV ( $\mu\text{m}$ )
1H01W15.5	0.16	83	10	57	32	44	220	12	nd
1H01W44	0.44	81	10	59	30	44	225	12	nd
1H01W73	0.73	47	12	69	18	43	13	242	nd
1H01W112	1.12	40	13	70	17	44	13	nd	nd
1H02W6.5	1.57	36	12	74	14	42	12	nd	nd
1H02W47	1.97	34	12	74	13	43	12	nd	nd
1H02W84.5	2.35	33	14	72	14	43	11	nd	nd
1H02W124	2.74	38	12	72	16	44	11	nd	nd
1H03W7	3.07	43	13	69	19	43	12	201	nd
1H03W46	3.46	61	12	63	25	46	12	344	nd
1H03W86	3.86	59	15	61	23	41	13	339	nd
1H03W116	4.16	63	21	55	24	10	2	43	342
1H03W147	4.47	48	30	50	19	2	7	42	223
1H04W44	4.94	59	24	53	22	3	8	43	339
1H04W76	5.26	49	39	38	23	2	9	168	43
1H04W140	5.90	52	21	50	28	143	10	3	48
1H05W17	6.17	48	19	49	31	109	10	3	nd
1H05W43	6.43	51	21	48	31	116	10	3	nd
1H05W96	6.96	51	22	45	33	114	2	9	nd
1H05W142	7.42	51	21	45	34	103	2	9	nd

Modes I–IV represent the highest % grain-size (mean value is given), in descending order of dominance. The descriptors follow the scale of [Wentworth \(1922\)](#).

nd = no mode detected.

that the initial concentration of  $^{10}\text{Be}$  will also vary. The  $^{10}\text{Be}/^9\text{Be}$  ratio of deep Pacific Ocean water, in contrast, is relatively constant on a regional basis ([von Blanckenburg and Igel, 1999](#)), and has appeared to vary little over the past ca. 12 Ma ([Ling et al., 1997](#)). Beryllium should, therefore, be adsorbed into hydrogenous ferromanganese nodules at a relatively constant isotopic ratio, irrespective of the rate of incorporation.

For the sediment in the core, it is likely also that beryllium will be incorporated in widely varying amounts depending on the sedimentation rate, composition of the sediment, water chemistry, etc. Although the  $^{10}\text{Be}/^9\text{Be}$  ratio of any adsorbed beryllium should be equivalent to contemporary seawater values, that of the total sediment might not be due to the presence of pre-existing detrital silicate material. The latter could, during sample preparation leaching, contribute older, decayed, beryllium to the measured ratios, an issue we discuss further in [Section 5](#). Notwithstanding this possibility, we may reasonably assume that both the ferromanganese nodules and the entrapping

sediments remain closed systems with respect to beryllium subsequent to formation, due to beryllium's low mobility under weakly acidic to alkaline conditions (i.e.  $\text{pH} > 5$ ) ([Li, 1982](#); [Mangini et al., 1986](#)).

### 3. Analytical results

#### 3.1. Methods

All samples for analysis were obtained from Unit IA (Hole B, 1H and 2H), and were curated in a controlled, clean air environment prior to shipping. Sediment and ferromanganese nodule samples were kept separate during all stages of handling and processing, to avoid cross-contamination.

Five of the larger nodules (i.e. 3–8 cm diameter) were bisected, and one hemisphere of each used for analysis. Using a mini diamond saw, 0.4–0.6 g sub-samples from each nodule were carved out parallel to the growth layers and reduced to pow-

der with an agate pestle and mortar. Fifty-two 5–10 g sediment samples to 15.34 mbsf were analysed, at an average sampling interval of ca. 0.3 m. Relatively large samples were processed, particularly from deep in the sediment core (i.e. below 5 mbsf), to ensure the leachates contained sufficient  $^9\text{Be}$  and  $^{10}\text{Be}$  for separate, precise analysis.

Chemical preparation methods used for beryllium isotopic analysis of ferromanganese nodules and deep-sea marine sediments are detailed in Ditchburn and Graham (2003). In summary, powdered sub-samples were leached for 30 min (nodules) or 1 h (sediment) in hot 6 M HCl, then sub-sampled for measurement of natural  $^9\text{Be}$  by ICP–OES. The latter is a custom-built instrument that can resolve spectral interference from vanadium and titanium in the sample matrix, and yields 2% relative precision ( $1\sigma$ ). One mg of BDH  $^9\text{Be}$  carrier ( $^{10}\text{Be}/^9\text{Be} \approx 10^{-14}$  atom

atom $^{-1}$ ) was then added to the remaining leachate, and beryllium for  $^{10}\text{Be}$  analysis extracted by hydroxide precipitation and cation exchange chromatography.

Accelerator Mass Spectrometry (AMS) measurements of  $^{10}\text{Be}$  were made at the National Isotope Centre, Institute of Geological and Nuclear Sciences, New Zealand, using a MC–SNICS caesium-sputtering ion source (Zondervan, 2001). The EN-tandem accelerator was operated near 5.5 MV, and the 3+ charge state obtained via a carbon-foil stripper at the terminal. Interference from the stable isobar  $^{10}\text{B}$  during the detection of  $^{10}\text{Be}$  was minimised by the use of an absorber cell in front of the gas-ionisation detector. Interference from  $^7\text{Be}$ , produced by the nuclear reaction  $^{10}\text{B}(^1\text{H}, ^4\text{He})^7\text{Be}$ , was accounted for via measurement on a cathode position that contained  $^9\text{Be}$  carrier, with ca. 0.1% by weight boron added to it. The NIST standard SRM4325,  $^{10}\text{Be}/$

Table 2  
Analytical data for ferromanganese nodules from Site 1121 sediment core

Sample field number	Sample range (mm) <sup>a</sup>	Centre of interval (mm) <sup>b</sup>	$^{10}\text{Be}/^9\text{Be}$ ( $10^{-7}$ atom atom $^{-1}$ ) <sup>c</sup>	$^{10}\text{Be}$ ( $10^9$ atoms g $_{\text{total}}^{-1}$ ) <sup>d</sup>	$^9\text{Be}$ ( $\mu\text{g g}_{\text{total}}^{-1}$ ) <sup>d</sup>	Insoluble residue (%) <sup>e</sup>
1H01W0/1	0.0–3.0	1.38	1.19 ± 0.09	13.90	1.75	30.5
1H01W0/2	4.0–7.0	5.37	0.67 ± 0.05	14.18	3.16	30.3
1H01W0/3	8.0–10.5	9.14	0.43 ± 0.03	10.62	3.74	33.4
1H01W0/4	11.2–16.3	13.23	0.27 ± 0.02	8.08	4.55	33.3
1H01W0/5	17.4–23.0	18.77	0.19 ± 0.01	6.49	5.11	31.6
1H01W10/1	0.0–2.8	1.29	0.61 ± 0.05	9.29	2.29	35.0
1H01W10/2	3.8–8.2	5.63	0.43 ± 0.03	10.06	3.47	37.4
1H01W10/3	9.1–15.1	10.89	0.25 ± 0.02	7.69	4.59	34.8
1H01A142/1	0.0–3.4	1.49	0.22 ± 0.02	4.90	3.33	38.1
1H01A142/2	4.6–10.2	6.46	0.15 ± 0.01	4.32	4.37	41.2
1H03W14/1	0.0–3.0	1.44	0.095 ± 0.007	2.49	3.93	44.5
1H03W14/2	4.0–9.0	6.30	0.074 ± 0.005	2.44	4.95	44.0
1H03W14/3	10.0–12.0	10.96	0.055 ± 0.004	1.55	4.25	42.6
1H03W14/4	13.0–18.0	15.25	0.043 ± 0.003	1.48	5.14	27.1
1H03W14/5	19.0–22.0	20.39	0.029 ± 0.002	1.09	5.58	25.9
1H03W14/6	23.5–32	26.39	0.021 ± 0.002	0.70	4.92	42.6
1H03W105/1	0.0–2.7	1.26	0.0112 ± 0.0008	0.28	3.67	44.5
1H03W105/2	3.6–7.9	5.41	0.0103 ± 0.0008	0.31	4.51	44.8
1H03W105/3	8.4–10.8	9.42	0.0100 ± 0.0008	0.34	5.06	27.2
1H03W105/4	11.5–15	nd	0.0072 ± 0.0006	0.20	4.12	39.8

<sup>a</sup> Measured from the outer rim towards the nodule nucleus.

<sup>b</sup> Calculated from the sample range after correcting for outward bias due to radiometric decay and for sampling spheroidal growth surfaces.

<sup>c</sup>  $2\sigma$  precision.

<sup>d</sup> Concentration in leachate per g total sample.

<sup>e</sup> Amount of dry sample remaining after leaching.

Table 3  
 $^{10}\text{Be}/^9\text{Be}$  ages of ferromanganese nodules from Site 1121 sediment core

Sample field number	Depth in core (mbsf)	Nodule radius (mm)	Nodule core age (Ma)	Nodule rim age (Ma)	Nodule growth span (m.y.)	Nodule growth rate (mm m.y. <sup>-1</sup> )
1H01W0	0.03	23.0	4.8 ± 0.3	-0.1 ± 0.2	4.9 ± 0.4	4.7 ± 0.3
1H01W10	0.12	16.8	4.8 ± 0.3	1.4 ± 0.2	3.4 ± 0.5	4.9 ± 0.4
1H01A142	1.43	13.0	5.9 ± 0.4	3.7 ± 0.2	2.2 ± 0.6	5.7 ± 1.2
1H03W14	3.18	37.0	10.5 ± 0.2	5.5 ± 0.1	5.0 ± 0.3	7.5 ± 0.4
1H03W105	4.08	15.0	10.9 ± 0.2	10.4 ± 0.2	0.5 ± 0.4	[32 ± 12] <sup>a</sup>

Nodule core ages and nodule rim ages are derived from projections of measured  $^{10}\text{Be}/^9\text{Be}$  values to the nodule nucleus and rim, respectively, and assuming a constant initial  $^{10}\text{Be}/^9\text{Be}$  ratio equal to SWPO sea water,  $(1.336 \pm 0.052) \times 10^{-7}$  atom atom<sup>-1</sup>.

<sup>a</sup> Based only on the outer three data (see Table 2; Fig. 2).

$^9\text{Be} = (3.06 \pm 0.14) \times 10^{-11}$  atom atom<sup>-1</sup> (Middleton et al., 1993), was used for normalisation and to correct for instrumental drift. Analytical errors from Poisson counting statistics and instrumental variability were combined for each sample to a single accuracy figure.

### 3.2. Entrapped nodules

The analysed nodules all had rough outer surfaces, spheroidal, flattened elongate or polynodular shapes, and indistinct banded internal structures. Two to six sub-samples per nodule were analysed (Table 2). These proved to be of sufficient number, and the analytical data of sufficiently high precision, to provide useful age information (Table 3), namely, a *nodule core age* (the initiation of nodule growth), a *nodule rim age* (the cessation of nodule growth), and a *nodule growth span* (the time period of nodule growth). Nodule core ages and nodule rim ages were calculated by extrapolation of measured  $^{10}\text{Be}/^9\text{Be}$  ratios to the actual core and rim of the nodules, respectively (Fig. 2), taking into account: (1) changes in growth rate, (2) outward bias of the sampling interval due to exponential weighting by the radiometric decay curve, (3) outward bias of the sampling interval due to the effect of sampling spheroidal volume segments, and (4) measurement uncertainties (see Graham et al., 2003, for a fuller explanation). The extrapolated  $^{10}\text{Be}/^9\text{Be}$  ratios were converted to ages using a constant value for  $^{10}\text{Be}/^9\text{Be}$  at the time of formation,  $(1.34 \pm 0.05) \times 10^{-7}$  atom atom<sup>-1</sup> (SWPO seawater). This value was determined from eight ferromanganese

nodules recovered from the Campbell Nodule Field (Graham et al., 2003), and is similar to the long-term mean value for Pacific Ocean seawater quoted by Ling et al. (1997). (But note that von Blanckenburg and Igel, 1999, obtained a somewhat lower value of  $(1.10 \pm 0.14) \times 10^{-7}$  atom atom<sup>-1</sup>, the variance being due presumably to inter-laboratory calibration differences.) The uncertainty in the SWPO seawater value has been propagated into the final age uncertainties of the five entrapped nodules, but no account has been taken of possible variation in that value through time (for which there is as yet scant information).

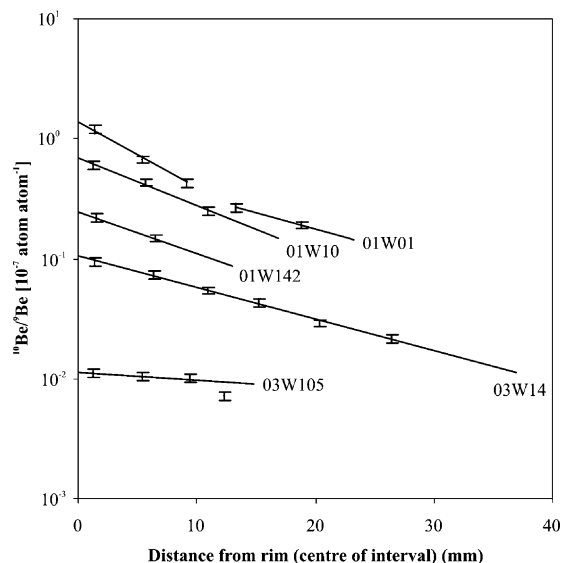


Fig. 2.  $^{10}\text{Be}/^9\text{Be}$  profiles of entrapped nodules from Site 1121 sediment core (extrapolated to the nodule rim and core). Error bars are  $2\sigma$ .

Both the core and rim ages of the nodules decrease systematically towards the top of the sediment core (Table 3). Nodule core ages range from 10.9 to 4.8 Ma, while nodule rim ages range from 10.4 to 0 Ma. It should be noted that the inherent accuracy of the nodule core ages is considerably less than for the nodule rim ages, because: (1) the inner part of the nodule, being older, has lower

$^{10}\text{Be}/^9\text{Be}$ , which is analysed typically at lower precision, (2) inner samples are more difficult to extract accurately with respect to the growth layers, and (3) the nodule nucleus is often obscure and difficult to locate with certainty, making the inner extrapolation point less certain than the rim.

### 3.3. Sediments

The  $^{10}\text{Be}$  atoms  $\text{g}_{\text{total}}^{-1}$  and  $^{10}\text{Be}/^9\text{Be}$  profiles for the sediment samples are closely similar (Fig. 3A) and overall decrease with depth in accordance with radioactive decay. The isotopic ‘reversals’ below ca. 7 mbsf are due, in part, to analytical uncertainties which range from ca. 20% ( $2\sigma$ ) to  $>100\%$  near the detection limit for  $^{10}\text{Be}$  (Table 4). A first-pass geochronological interpretation of the  $^{10}\text{Be}/^9\text{Be}$  data, assuming a constant initial ratio equal to SWPO seawater, yields an age for the sediment core to 7 mbsf of ca. 18 Ma, and indicates a decrease in overall sedimentation rate towards the top. This, however, is too simplistic an interpretation, since it fails to properly explain either the variations in the isotopic profile, or the ages of the entrapped nodules.

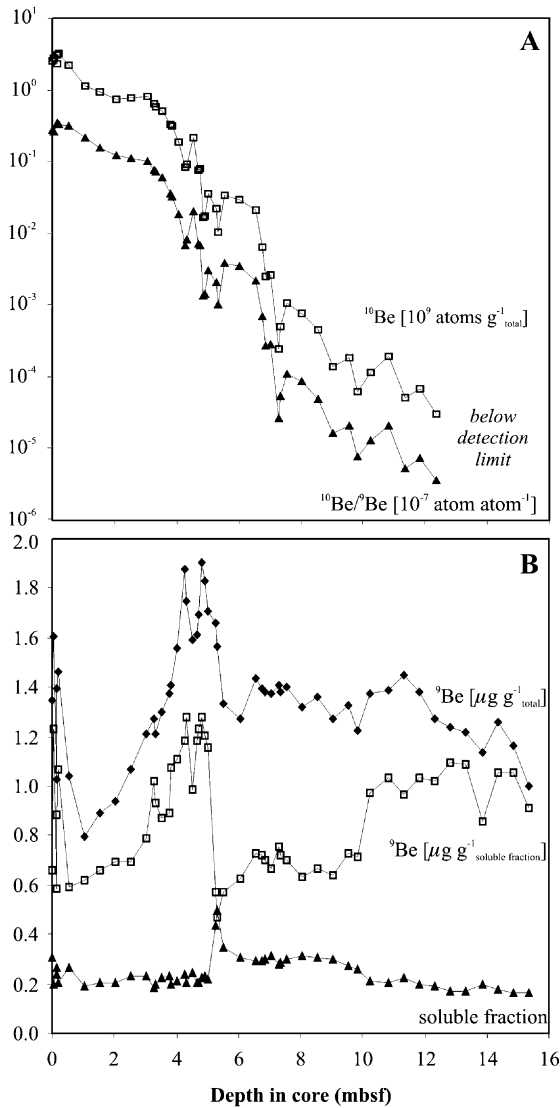


Fig. 3. Depth profiles for the Site 1121 sediment core. (A)  $^{10}\text{Be}$  atoms  $\text{g}_{\text{total}}^{-1}$  and  $^{10}\text{Be}/^9\text{Be}$ . (B)  $^9\text{Be}$   $\mu\text{g g}_{\text{total}}^{-1}$ ,  $^9\text{Be}$   $\mu\text{g g}_{\text{soluble fraction}}^{-1}$  (scaled to 15% of actual values) and soluble fraction.

## 4. Chronology of the entrapped nodules

The rim ages of the entrapped nodules provide the best available indication of the absolute age of the Site 1121 sediment core to ca. 4 mbsf. In the following discussion, we will explore this assertion by considering the origin of the nodules, and their likely behaviour during and after growth.

### 4.1. Mode of formation of the entrapped nodules

The non-botryoidal surface textures and relatively slow growth rates of the entrapped nodules indicate that they are essentially hydrogenous in origin, growing largely above the seafloor (von Stackelberg, 1987). To maintain this mode of growth for up to ca. 5 m.y. (cf. nodule growth span in Table 3), the nodules must have formed during a period of low net sediment accumulation in conditions of relatively high biogenic activity (von Stackelberg and Marchig, 1987, fig. 26). Fer-

romanganese nodules grow, at least partly, through bacterial activity, and serve as a substratum and place of refuge for sessile micro-organisms (Janin, 1987). The surfaces of nodules are therefore continuously attacked by feeding organisms, in an almost symbiotic relationship, which keeps them in a state of constant movement. This ‘biogenic lifting’ maintains their location near the seafloor, and may perhaps cause them to move small distances laterally (von Stackelberg, 1984, 1997; Weber et al., 2000). The relatively small size and short growth spans of the Site 1121 nodules suggest they are mainly juveniles that were trapped during periods when sediment accumulation was too rapid for biogenic lifting to maintain buoyancy (von Stackelberg, 1987).

#### 4.2. Relationship to seafloor nodules of the Campbell Nodule Field

All of the entrapped nodules in the Site 1121 sediment core are much smaller (30–60 mm long axis) than the seafloor nodules of the Campbell Nodule Field (60–220 mm long axis) analysed by Graham et al. (2003), and yield correspondingly lower growth spans (0.5–5.0 m.y. vs. 6.4–14.9 m.y.). Both sets of nodules have similarly slow growth rates (7.5–4.7 mm m.y.<sup>-1</sup> vs. 6.9–3.5 mm m.y.<sup>-1</sup>), typical of hydrogenous growth. Growth rates of the entrapped nodules decrease uniformly towards the top of the sediment core (Table 3), which is similar, in a temporal sense, to the core-rim decrease in growth rate shown by the larger (i.e. older) nodules of the Campbell Nodule Field. <sup>9</sup>Be concentrations and % residue (i.e. non-acid-soluble silicate material) are similar in range, and both sets of nodules show characteristic reductions in <sup>9</sup>Be concentration towards the nodule rims (Table 2). These similarities confirm that the entrapped nodules are representative of, and partially record the history of, the Campbell Nodule Field at this locality.

#### 4.3. Interpretation of the nodule rim ages

In a detailed study of hydrogenous nodules entrapped in sediments in the equatorial North Pacific, von Stackelberg (1987) inferred from phys-

ical appearance, mineralogy and chemistry that only minimal dissolution must have taken place after burial. The final phase of rapid diagenetic growth in those nodules occurred at a burial depth of a few cm, immediately before the Eh-minimum (i.e. the boundary of the reducing zone) passed by as it moved upwards due to rapid burial. Beneath the Eh-minimum, nodule growth ceased, and the delicate outermost nodule layer was preserved for the ensuing several m.y. The similarity in growth rates, <sup>9</sup>Be concentrations and % residue profiles of the entrapped nodules with those of their seafloor counterparts in the Campbell Nodule Field, as well as their external physical appearance, suggests that they too have retained their original form, i.e. they have lost none of their mass through surface corrosion or dissolution. Thus, we believe that the nodule rim ages truly represent the time that the nodules ceased growing.

Assuming that the nodules grew to their observed form at or close to the contemporary seafloor, several interpretations for their rim ages are possible:

- they represent the timing of sedimentation, i.e. the nodules are intact and were entrapped as a result of being overcome by sedimentary processes;
- they are younger than the encasing sediment, i.e. the nodules are deeper than they should be because of corer impact, or through settling into soft sediment;
- they are older than the encasing sediment, i.e. the nodules are shallower than they should be through extreme bioturbation.

The projected rim <sup>10</sup>Be/<sup>9</sup>Be ratio of the topmost nodule ( $1.36 \pm 0.1 \times 10^{-7}$ ) is within 1σ of the SWPO seawater value, which indicates that it was still growing when the sediment core was extracted. There is no physical evidence that any of the other nodules have sunk significantly into the sediment; given that deep-sea sediment is relatively dense and viscous, it is unlikely any of the nodules would sink more than a few centimetres after burial, either naturally or by corer impact. There is also no physical evidence for extreme bioturbation in the parts of the core containing nodules. Thus, we may reasonably assume that

the nodules are in situ, and the derived nodule rim ages represent the actual age of the sediment at their respective locations in the sediment core.

#### 4.4. Interpretation of the nodule core ages

We have judged that the buried nodules are hydrogenous in origin, and therefore formed just above the sediment–seawater interface by accretionary precipitation from Fe–Mn-charged seawater. If this had occurred at the actual Site 1121 location, it might be expected that individual nodules within the sediment column would have rim ages older than the core ages of nodules stratigraphically above them. However, this is not the case for any of the analysed nodules (Table 3). There are two possible explanations for this: (1) the nodules continued to accrete from pore fluids some time after they were covered in sediment, and (2) the nodules began growing somewhere else, and were re-located to Site 1121 by seafloor sedimentary processes. Explanation (1), which would imply that the nodule rim ages do not give the true age of sedimentation, is very unlikely to be true. The significant distances between the lower three nodules in the core (0.90 m and 1.75 m, respectively) means that these nodules would have had to have continued growing for some considerable time after being buried by ca. 1 m or more of sediment. Analysis of ‘unusual’ capped nodules recovered from the Campbell Nodule Field (Graham et al., 2003) indicates that their undersides effectively ceased growing when buried by just a few cm of sediment. This is consistent with the inference of von Stackelberg (1987) that even diagenetic growth can only occur in the top few cm of sediment. Hence, we favour explanation (2), which implies that the nodules must have originated somewhere nearby in the Campbell Nodule Field (perhaps on a submarine hill-crest; von Stackelberg, 1987), before being transported to and entrapped in the Site 1121 sedimentary pile. This does not seem unreasonable, given the relatively small size of the nodules, and the strong currents acting in this region (Carter and McCave, 1997). If so, then the cores of the buried nodules could be of any age up to that of the initiation of the Campbell Nodule Field. The

nodules must have been transported to the Site 1121 location some time after initiation of growth, and prior to cessation of growth (i.e. burial). In the case of the uppermost nodules, this must have been well after initiation of growth, given the degree of overlap with the subjacent nodule core age (Table 3). It is significant, however, that the nodule core ages show progressive increases in age with depth in the core, suggesting that the transporting process was only able to move small, juvenile nodules at specific times during the past ca. 11 m.y.

## 5. Chronology of the sediment samples

If one accepts the chronostratigraphy for the sediment core as derived from the entrapped nodules, then it is not possible to interpret the sediment data in any simple way. Although the sediment samples show an overall decay profile, the  $^{10}\text{Be}/^9\text{Be}$  data are in agreement with the rims of the entrapped nodules only between ca. 4 and 3 mbsf. Nearer the top of the core the sediment  $^{10}\text{Be}/^9\text{Be}$  ratios are consistently lower, yielding a seafloor intercept value significantly less than that of SWPO seawater. There are several possible explanations for this.

### 5.1. Variable extraction of $^9\text{Be}$ during leaching?

The conventional approach to dating marine sediments using beryllium isotopes is to attempt to extract and analyse only the beryllium in equilibrium with contemporary seawater (i.e. the authigenic component), while excluding any beryllium from detrital sources. Various complicated leaching methods using weak acids and/or alkalis (e.g.  $\text{MgCl}_2$ ,  $\text{NaOAc}$ ,  $\text{NH}_2\text{OH}\cdot\text{HCl}$  in  $\text{HOAc}$ ,  $\text{H}_2\text{O}_2$ ,  $\text{NH}_4\text{OAc}$  in  $\text{HNO}_3$ ) have been employed to this end (e.g. Bourlès et al., 1989). However, these have often given rise to ambiguous interpretations. Bourlès et al. (1989) found a generally poor agreement between the authigenic  $^{10}\text{Be}/^9\text{Be}$  age and the palaeomagnetic age of sediment core RC12-65 (central Pacific Ocean), and concluded that  $^{10}\text{Be}/^9\text{Be}$  measurements of the total sample (authigenic+detrital) yielded more consistent re-

Table 4  
Analytical data for Site 1121 sediment

Sample field number	Depth in core (mbsf)	$^{10}\text{Be}/^9\text{Be}$ ( $10^{-7}$ atom atom $^{-1}$ ) <sup>b</sup>	$^{10}\text{Be}$ ( $10^9$ atoms $\text{g}_{\text{total}}^{-1}$ )	$^9\text{Be}$ ( $\mu\text{g } \text{g}_{\text{total}}^{-1}$ )	Soluble fraction <sup>a</sup>
1H01W0	0.01	0.28 ± 0.007	2.49	1.35	0.31
1H01W6	0.07	0.25 ± 0.007	2.73	1.61	0.20
1H01W13	0.14	0.34 ± 0.013	2.35	1.03	0.26
1H01W14	0.15	0.33 ± 0.008	3.12	1.40	0.24
1H01W14 <sup>f</sup>	0.15	0.79 ± 0.036	4.84	0.92	0.26
1H01W14 <sup>c</sup>	0.15	0.25 ± 0.011	2.40	1.41	0.21
1H01W14 <sup>td</sup>	0.15	0.0063 ± 0.0003	0.061	1.46	na
1H01W18	0.19	0.33 ± 0.008	3.23	1.46	0.20
1H01W53	0.54	0.31 ± 0.014	2.16	1.04	0.26
1H01W103	1.04	0.21 ± 0.010	1.14	0.80	0.19
1H02W3	1.54	0.16 ± 0.007	0.94	0.89	0.20
1H02W53	2.04	0.12 ± 0.006	0.75	0.94	0.20
1H02W103	2.54	0.11 ± 0.005	0.77	1.07	0.23
1H03W3	3.04	0.10 ± 0.005	0.80	1.21	0.23
1H03W27	3.28	0.076 ± 0.002	0.65	1.27	0.19
1H03W27 <sup>f</sup>	3.28	0.087 ± 0.003	0.92	1.58	0.24
1H03W27 <sup>c</sup>	3.28	0.056 ± 0.003	0.48	1.29	0.16
1H03W27 <sup>td</sup>	3.28	0.0020 ± 0.0001	0.019	1.41	na
1H03W34	3.34	0.072 ± 0.002	0.58	1.21	0.20
1H03W53	3.54	0.059 ± 0.003	0.52	1.30	0.22
1H03W77	3.78	0.036 ± 0.001	0.33	1.38	0.23
1H03W83	3.84	0.033 ± 0.001	0.31	1.41	0.20
1H03W103	4.04	0.018 ± 0.001	0.19	1.56	0.21
1H03W127	4.28	0.0068 ± 0.0002	0.085	1.88	0.24
1H03W131	4.32	0.0080 ± 0.0002	0.093	1.75	0.21
1H04W3	4.54	0.0200 ± 0.0010	0.218	1.59	0.24
1H04W17	4.68	0.0071 ± 0.0002	0.077	1.61	0.21
1H04W23	4.74	0.0069 ± 0.0002	0.078	1.69	0.21
1H04W33	4.84	0.0013 ± 0.0001	0.017	1.90	0.22
1H04W39	4.90	0.0014 ± 0.0001	0.017	1.83	0.23
1H04W53	5.04	0.0031 ± 0.0002	0.035	1.71	0.22
1H04W77	5.28	0.0020 ± 0.0001	0.022	1.66	0.44
1H04W81	5.32	0.0010 ± 0.0001	0.010	1.56	0.50
1H04W103	5.54	0.0038 ± 0.0002	0.034	1.33	0.35
1H05W3	6.04	0.0034 ± 0.0002	0.029	1.27	0.31
1H05W53	6.54	0.0022 ± 0.0001	0.021	1.43	0.29
1H05W77	6.78	0.00068 ± 0.00006	0.0064	1.40	0.29
1H05W84	6.85	0.00027 ± 0.00003	0.0025	1.38	0.30
1H05W103	7.04	0.00029 ± 0.00004	0.0026	1.37	0.31
1H05W127	7.28	0.00002 ± 0.00003	0.0002	1.41	0.28
1H05W135	7.36	0.00005 ± 0.00002	0.0005	1.38	0.29
1H06W3	7.54	0.00011 ± 0.00002	0.0010	1.40	0.30
1H06W53	8.04	0.00008 ± 0.00002	0.0007	1.32	0.31
1H06W103	8.54	0.00005 ± 0.00001	0.0004	1.36	0.31
1H07W3	9.04	0.00002 ± 0.00001	0.0001	1.27	0.30
1H07W53	9.54	0.00002 ± 0.00001	0.0002	1.33	0.27
2H 01W13	9.84	0.00001 ± 0.00001	0.0001	1.22	0.26
2H 01W63	10.24	0.00001 ± 0.00001	0.0001	1.37	0.21
2H 01W113	10.84	0.00002 ± 0.00001	0.0002	1.39	0.20
2H 02W13	11.34	nd	nd	1.45	0.23
2H 02W63	11.84	nd	nd	1.38	0.20
2H 02W113	12.34	nd	nd	1.28	0.19

Table 4 (Continued).

Sample field number	Depth in core (mbsf)	$^{10}\text{Be}/^9\text{Be}$ ( $10^{-7}$ atom atom $^{-1}$ ) <sup>b</sup>	$^{10}\text{Be}$ ( $10^9$ atoms $\text{g}_{\text{total}}^{-1}$ )	$^9\text{Be}$ ( $\mu\text{g g}_{\text{total}}^{-1}$ )	Soluble fraction <sup>a</sup>
2H 03W13	12.84	nd	nd	1.24	0.17
2H 03W63	13.34	nd	nd	1.22	0.17
2H 03W113	13.84	nd	nd	1.14	0.20
2H 04W13	14.34	nd	nd	1.26	0.18
2H 04W63	14.84	nd	nd	1.16	0.17
2H 04W113	15.34	nd	nd	1.00	0.16

<sup>f</sup> = fine fraction and <sup>c</sup> = remaining coarse fraction, after separation of fines.

<sup>td</sup> = total decomposition of residue, after 6 M HCl leaching of original sample.

na = not applicable.

nd = not determined ( $^{10}\text{Be}$  below detection limit).

<sup>a</sup> Proportion of total sample dissolved during leaching.

<sup>b</sup>  $2\sigma$  precision.

sults. This was ascribed to gradual diagenesis of the sediment with depth (and/or time), resulting in a progressive equilibration of the beryllium isotopes in situ. Noting these observations, Henken-Mellies et al. (1990) used cold 6 M HCl to leach deep-sea sediments from DSDP 519, claiming to have extracted mainly authigenic beryllium in the process.

We chose to leach our samples with hot 6M HCl to ensure complete extraction of  $^{10}\text{Be}$ . As a check on the effectiveness of this, two residues after leaching (1H1W14 and 1H03W27) were totally decomposed and analysed. These yielded  $^{10}\text{Be}$  concentrations amounting to 1.5% and 2.4%, respectively, of the leachate (Table 4), which can be attributed largely to residual leachate unable to be washed out of the residue. Much higher levels of  $^9\text{Be}$  remained in the residue (79% and 90%, respectively), in contrast to the results of Henken-Mellies et al. (1990). Hot 6M HCl leaching does, therefore, have the potential to extract non-equilibrium beryllium from the sediment and, if this occurred to a significant (and variable) extent, the calculated  $^{10}\text{Be}/^9\text{Be}$  ages (based on a fixed initial  $^{10}\text{Be}/^9\text{Be}$  ratio) would be suspect. However, as we will show, the sediment beryllium isotope story has complexities which are largely independent of the leaching method employed.

If the observed sediment  $^{10}\text{Be}/^9\text{Be}$  profile is simply a reflection of variable extraction of  $^9\text{Be}$  from detrital minerals, then we might expect to find a positive correlation between  $^9\text{Be}$   $\mu\text{g g}_{\text{total}}^{-1}$  (i.e. the

$^9\text{Be}$  concentration in the leachate per g of total sample) and soluble fraction (i.e. the fraction of sediment dissolved during leaching). This would result in a flat trend in  $^9\text{Be}$   $\mu\text{g g}_{\text{soluble fraction}}^{-1}$  (i.e. the  $^9\text{Be}$  concentration in the leachate per g of soluble component). However, we find no such correlation for most of the sediment core (Fig. 3B), which suggests that the high concentrations of  $^9\text{Be}$  observed in the sediment residues (cf. 1H01H14<sup>td</sup> and 1H03W27<sup>td</sup> in Table 4) are locked into mineral lattices, and not subject to leaching.

In detail, there appear to be a number of different processes at work. From ca. 12.5 to 7 mbsf,  $^9\text{Be}$   $\mu\text{g g}_{\text{total}}^{-1}$  increases by ca. 10% (Fig. 3B) whereas the soluble fraction increases by 70%, resulting in a steady decline in  $^9\text{Be}$   $\mu\text{g g}_{\text{soluble fraction}}^{-1}$ . This indicates a decrease in the leachability of beryllium, due either to a reduction in the degree of diagenetic alteration (Bourlès et al., 1989) or a gradual change in sediment composition (or both). From ca. 7 to 5 mbsf, a rapid drop in  $^9\text{Be}$   $\mu\text{g g}_{\text{soluble fraction}}^{-1}$  is accompanied by a rapid increase in soluble fraction, which coincides with an influx of soluble phosphate (Fig. 4) containing significantly less beryllium than soluble silicate. (Note that a phosphatic concretion at 5.41 mbsf yielded only  $1.5 \mu\text{g g}^{-1} ^9\text{Be}_{\text{total}}$ , and no detectable  $^{10}\text{Be}$ . It must have been redeposited from an older substrate some distance away from Site 1121, given that the 30–50% sediment component of the concretion should have had detectable levels of  $^{10}\text{Be}$  at this depth in the core, if it had formed in situ.) From ca. 5 to 1 mbsf, there is an initial

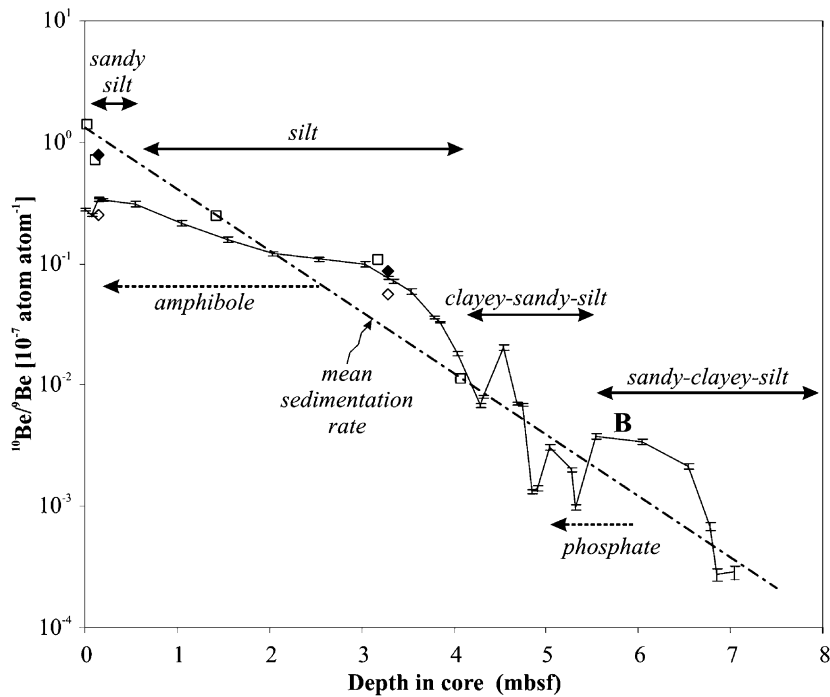


Fig. 4.  $^{10}\text{Be}/^9\text{Be}$  vs. depth to 7.04 mbsf for the Site 1121 sediment core. Error bars for the sediment data are  $2\sigma$ . Filled diamonds are fine fractions and open diamonds are coarse fractions of sediment samples 1H1W14 (0.15 mbsf) and 1H03W27 (3.28 mbsf), respectively. Open squares are rim compositions of entrapped ferromanganese nodules. The mean sedimentation rate is based on the rim age of the deepest nodule. 'B' indicates a zone of relatively intense bioturbation.

sharp increase in  $^9\text{Be}$   $\mu\text{g g}_{\text{soluble fraction}}^{-1}$  to the highest values recorded, followed by a steady decline. Through this segment of the core, where the initial  $^{10}\text{Be}/^9\text{Be}$  ratio progressively departs from that of contemporary seawater,  $^9\text{Be}$   $\mu\text{g g}_{\text{total}}^{-1}$  also declines steadily while the soluble fraction remains invariant. Here, the  $^9\text{Be}$  concentration, and thus the  $^{10}\text{Be}/^9\text{Be}$  ratio, must be reflecting compositional change in the sediment. The two-fold decrease in  $^9\text{Be}$   $\mu\text{g g}_{\text{soluble fraction}}^{-1}$  indicates a reduction in the amount of total beryllium available for extraction in the soluble component. If the reduction in initial  $^{10}\text{Be}/^9\text{Be}$  from ca.  $1.3 \times 10^{-7}$  (seawater) at 4 mbsf to ca.  $0.3 \times 10^{-7}$  at the top of the core was largely due to changes in extraction of  $^9\text{Be}$  from the detrital component, then the  $^9\text{Be}$  concentration would have had to have increased more than four-fold. We actually observe a two-fold decrease.

The conclusion that variable  $^9\text{Be}$  extraction during sample processing is not primarily respon-

sible for the variability in the measured  $^{10}\text{Be}/^9\text{Be}$  ratios of the sediment can be confirmed by comparing  $^{10}\text{Be}/^9\text{Be}$  and  $^{10}\text{Be}$  atoms  $\text{g}_{\text{total}}^{-1}$  ages for the sediment (Fig. 5). These are calculated by applying the isotopic values for the topmost sediment sample, 1H01W0, to the standard age equation (Eq. 1). From ca. 7 mbsf to the top of the core, the  $^{10}\text{Be}/^9\text{Be}$  ages are the same as, or higher than the  $^{10}\text{Be}$  atoms  $\text{g}_{\text{total}}^{-1}$  ages, meaning that variation in the  $^{10}\text{Be}$  concentration, not the  $^9\text{Be}$  concentration, is causing the variability in  $^{10}\text{Be}/^9\text{Be}$  (e.g. from ca. 3 to 1 mbsf, the  $^{10}\text{Be}/^9\text{Be}$  age is lower, despite the rapid decline in  $^9\text{Be}$  concentration).

### 5.2. Variable beryllium isotopic composition of the soluble fraction

Atmospherically derived beryllium isotopes are transported through the water column to the seafloor in two main ways (McHargue and Damon, 1991; Li, 1991): (1) vertically via wind-blown

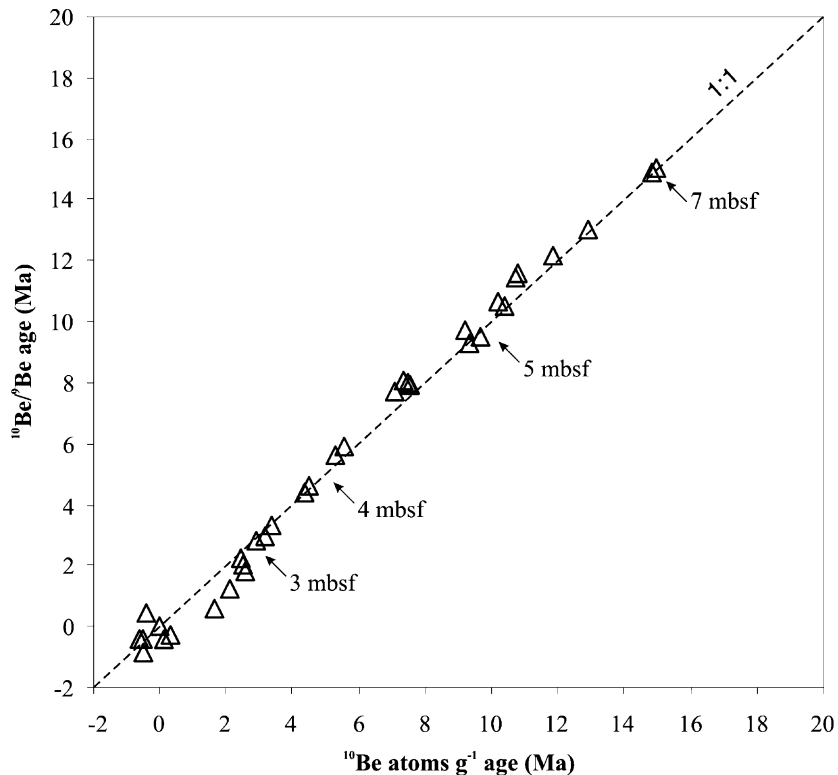


Fig. 5.  $^{10}\text{Be}/^9\text{Be}$  age vs.  $^{10}\text{Be}$  atoms  $\text{g}_{\text{total}}^{-1}$  age for Site 1121 sediment, calculated using the measured values for the top-most sample (1H01W0) as initial values. Approximate depths in the core are indicated.

aerosol and dust, organic matter, and Fe–Mn oxyhydroxides (authigenic component), and (2) horizontally via silicate detritus distributed by ocean currents (detrital component). In the open ocean, long residence times for beryllium of 500 years or more ensures that the authigenic component has a relatively constant  $^{10}\text{Be}/^9\text{Be}$  ratio close to that of contemporary seawater, particularly at deep oceanic levels (Kusakabe et al., 1987; von Blanckenburg and Igel, 1999). The detrital component, in contrast, will have variable  $^{10}\text{Be}/^9\text{Be}$ , depending on its age and origin and the degree of adsorption of beryllium isotopes onto reactive surfaces during transport through the water column. The sediment at Site 1121, therefore, would have initial  $^{10}\text{Be}/^9\text{Be}$  compositions equal to the resultant of the authigenic and detrital beryllium components, which might be significantly different from that of contemporary seawater.

Coarse detrital minerals in the leached residues

(abundant quartz with mica, plagioclase, K-feldspar) increase markedly towards the top of the sediment core (Table 6) and hornblende appears in samples at 2.54 mbsf and 0.54 mbsf, respectively. This is consistent with a gradual coarsening of the sediment (Table 1), and subtle colour changes. Wright et al. (2003) note that the Campbell Nodule Field has been subjected to increased terrigenous flux in recent times, related to breakthrough of the ACC (Fig. 1) through the Macquarie Ridge and erosion of the Solander fan (south of New Zealand) at ca. 3.3 Ma (Hall et al., 2001, 2002) and increased uplift and erosion of the Southern Alps since 5 Ma (Walcott, 1998). These events, together with changes to the flow of the DWBC should be reflected in sedimentation changes at Site 1121, although our dating would suggest that the initiation of these changes began earlier (at least 5.5 Ma, being the rim age of the nodule at 3.18 mbsf). We note that the changing

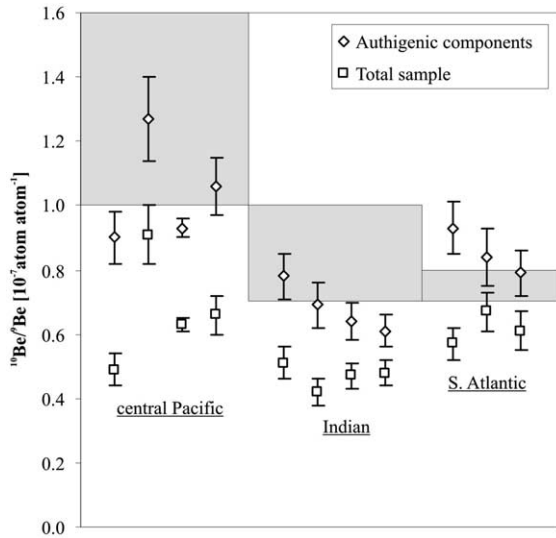


Fig. 6.  $^{10}\text{Be}/^9\text{Be}$  ratios of open ocean seafloor sediment samples from the central Pacific, Indian and South Atlantic oceans (Bourlès et al., 1989). Shaded areas are ranges of  $^{10}\text{Be}/^9\text{Be}$  in deep ocean water (after Bibvov Blanckenburg et al., 1996).

sediment composition is accompanied by a significant decrease in sedimentation rate (calculated from nodule rim ages), of ca. 95 to 8 cm m.y.<sup>-1</sup> (Table 7).

A gradual influx of coarse detritus, accompanied by a reduction in fines, is the most probable cause for the divergence in the measured  $^{10}\text{Be}/^9\text{Be}$  ratios of the sediment and nodule rims in the upper part of the sediment core. Deep sea sediment with a relatively high proportion of coarse detritus is unlikely to yield seawater  $^{10}\text{Be}/^9\text{Be}$  ratios, whatever leaching method is employed. Bourlès et al. (1989) analysed the authigenic component and total rock of 14 samples from the Pacific, Indian and Atlantic oceans, noting significant differences in the order of 32% (Fig. 6). While the  $^{10}\text{Be}/^9\text{Be}$  ratios of the authigenic component were broadly similar to mean sea water of their respective oceans, the total rock  $^{10}\text{Be}/^9\text{Be}$  ratios were ca. 42% less than mean seawater. Our leaching procedure should produce  $^{10}\text{Be}/^9\text{Be}$  ratios higher than total rock analyses, so the ca. 80% reduction in the  $^{10}\text{Be}/^9\text{Be}$  ratios of the near-seafloor sediments at Site 1121 is even greater than that observed by Bourlès et al. (1989). The

low initial  $^{10}\text{Be}/^9\text{Be}$  ratios at Site 1121 require that the two-fold reduction in  $^9\text{Be}$  concentration from ca. 4 mbsf be matched by an even greater (eight-fold) reduction in  $^{10}\text{Be}$  concentration. If the coarse detrital component causing these changes originated from progressively older deposits (i.e. more deeply eroded), then its  $^{10}\text{Be}/^9\text{Be}$  ratio could conceivably approach zero at the present day. To explain the  $^{10}\text{Be}/^9\text{Be}$  ratio of the top-most sediment sample, the coarse detrital component, at a

Table 5  
Model  $^{10}\text{Be}/^9\text{Be}$  ages of Site 1121 sediments

Sample field number	Depth in core (mbsf)	Model 1 age (Ma) <sup>a</sup>	Model 2 age (Ma) <sup>a,b</sup>
1H 01W0	0.01	0.1 ± 0.01	0.1 ± 0.01
1H 01W6	0.07	0.9 ± 0.02	0.9 ± 0.02
1H 01W13	0.14	1.5 ± 0.06	1.5 ± 0.06
1H 01W14	0.15	1.5 ± 0.04	1.5 ± 0.04
1H 01W18	0.19	1.6 ± 0.04	1.6 ± 0.04
1H 01W53	0.54	2.0 ± 0.1	2.0 ± 0.1
1H 01W103	1.04	2.8 ± 0.1	2.8 ± 0.1
1H 02W3	1.54	3.7 ± 0.2	3.7 ± 0.2
1H 02W53	2.04	4.5 ± 0.3	4.5 ± 0.3
1H 02W103	2.54	4.9 ± 0.3	4.9 ± 0.3
1H 03W3	3.04	5.3 ± 0.3	5.3 ± 0.3
1H 03W27	3.28	6.0 ± 0.3	6.0 ± 0.3
1H 03W34	3.34	6.1 ± 0.3	6.1 ± 0.3
1H 03W53	3.54	6.6 ± 0.4	6.6 ± 0.4
1H 03W77	3.78	7.8 ± 0.2	7.8 ± 0.2
1H 03W83	3.84	8.0 ± 0.2	8.0 ± 0.2
1H 03W103	4.04	9.2 ± 0.4	10.1
1H 03W127	4.28	11.4 ± 0.3	10.7
1H 03W131	4.32	11.0 ± 0.3	10.8
1H 04W3	4.54	9.0 ± 0.4	11.4
1H 04W17	4.68	11.3 ± 0.3	11.7
1H 04W23	4.74	11.3 ± 0.3	11.9
1H 04W33	4.84	14.9 ± 0.7	12.1
1H 04W39	4.90	14.8 ± 0.7	12.3
1H 04W53	5.04	13.1 ± 0.6	12.6
1H 04W77	5.28	14.0 ± 0.5	13.2
1H 04W81	5.32	15.5 ± 0.8	13.3
1H 04W103	5.54	12.6 ± 0.6	13.9
1H 05W3	6.04	12.9 ± 0.6	15.1
1H 05W53	6.54	13.9 ± 0.8	16.4
1H 05W77	6.78	16.3 ± 1.4	17.0
1H 05W84	6.85	18.4 ± 2.0	17.1
1H 05W103	7.04	18.2 ± 2.3	17.6

<sup>a</sup> 2σ precision, based on measurement uncertainties only.

<sup>b</sup> No errors given for samples from > 3.84 mbsf, since these are calculated using a fixed sedimentation rate of 39.2 cm m.y.<sup>-1</sup>.

Table 6  
XRD analysis of residues after acid leaching of Site 1121 sediment

Sample field number	Depth in core (mbsf)	Quartz	Mica	Plagioclase	K-feldspar	Amphibole	Kaolinite	Barite	Amorphous silica
1H1W53	0.54	A	T	M	M	T	nd	nd	M
1H2W103	2.54	A	T	M	M	T	T?	nd	M
1H04W53	5.04	A	T	M	M	nd	nd	nd	T
1H04W103	5.54	A	T	T	T	nd	nd	T	C
1H05W3	6.04	A	T	T	T	nd	nd	T	M
1H05W53	6.54	A	T	T	T	nd	nd	T	M
1H06W53	8.04	A	T	T	T	nd	T?	T	M

A = abundant (>60%); C = common (20–60%); M = minor (5–20%); T = trace (<5%) plagioclase is mainly albite; K-feldspar is mainly orthoclase; amphibole is mainly hornblende. nd = not detected.

$^{10}\text{Be}/^9\text{Be}$  ratio of zero, must provide at least 80% of the total beryllium measured, while this would rise to 100% if its  $^{10}\text{Be}/^9\text{Be}$  ratio was  $0.28 \cdot 10^{-7}$  atom atom<sup>-1</sup> (the maximum possible).

In order to assess whether the Site 1121 sediment might, in fact, comprise two components of contrasting beryllium isotopic composition, two samples (1H1W14 and 1H03W27) were split into coarse and fine fractions, and the two parts analysed separately (Table 4). In both cases, the fine fraction has a significantly higher  $^{10}\text{Be}/^9\text{Be}$  ratio than the total sample, and is similar to contemporary sea water values (Fig. 4). The sample nearer the top of the sediment core, in particular, demonstrates the increasingly dominant role of the coarse detrital component in reducing the measured  $^{10}\text{Be}/^9\text{Be}$  ratio below that of contemporary seawater. However, below ca. 3 mbsf, where the fine fraction dominates, the total sample has a  $^{10}\text{Be}/^9\text{Be}$  ratio indistinguishable from that of contemporary seawater.

Table 7  
Age spans and sedimentation rates for Site 1121 sediment core, based on Model 1 (Table 5)

Depth in core (mbsf)	Age span (m.y.)	Sedimentation rate (cm m.y. <sup>-1</sup> )
0.12–0.00	1.40	$8.2 \pm 0.9$
1.43–0.12	2.27	$58 \pm 8$
3.18–1.43	1.85	$95 \pm 15$
4.08–3.18	4.88	$18.5 \pm 1.2$
1.43–0.00	3.67	$39.0 \pm 2.2$
3.18–0.00	5.52	$57.6 \pm 1.3$
4.08–0.00	10.40	$39.2 \pm 0.8$

### 5.3. Model sediment ages

The chronology of the Site 1121 sediment samples is, therefore, best established by applying the assumption that the initial  $^{10}\text{Be}/^9\text{Be}$  ratio of the sediment was either: (1) contemporary seawater (i.e. the SWPO seawater value), or (2) a mixture of seawater and older, coarse detrital material (i.e. similar to the measured value of the surface sample 1H01W0). The first assumption applied to the entire sediment core yields an age for the near-surface samples of ca. 3.4 Ma, implying that,

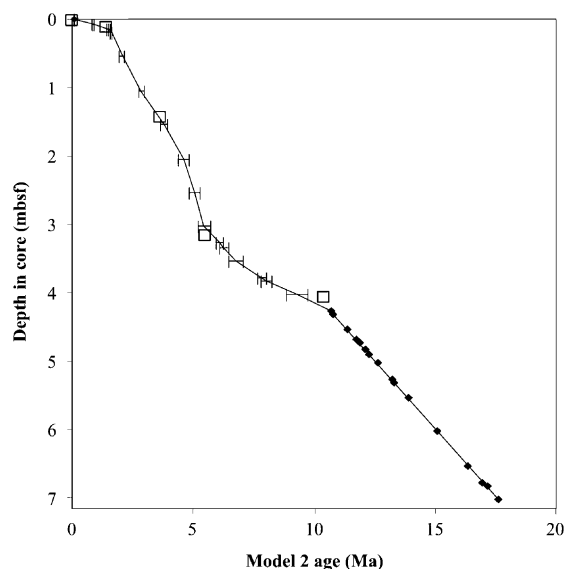


Fig. 7.  $^{10}\text{Be}/^9\text{Be}$  age vs. depth for Site 1121 sediment core. Filled Diamonds and error bars ( $2\sigma$ ) are sediment samples; open squares are nodule rim ages.

through erosion or by coring impact, the upper part of the sedimentary pile has been removed. (This, in principle could be verified or otherwise by determining the  $^{230}\text{Th}$  composition of the top-most sediment, but such an analysis was unable to be carried out.) The second assumption would imply that the near-surface samples are contemporary, and the rest of the sediment core is ca. 3.4 m.y. younger than if the first assumption were applied. Neither in itself explains the divergence of the nodule rim ages, which begins at ca. 3 mbsf (Fig. 3). The preferred interpretation, combining the nodule and sediment beryllium isotope data, is a combination of the two assumptions (i.e. Table 5, Model 1), applied as follows:

- below 3.54 mbsf, the initial  $^{10}\text{Be}/^9\text{Be}$  ratio of the sediment was SWPO seawater (i.e. the authigenic component is dominant);
- from 3.54 to 1.04 mbsf, the initial  $^{10}\text{Be}/^9\text{Be}$  ratio decreased systematically from the SWPO

seawater value to ca.  $0.8 \times 10^{-7}$ , with increasing dominance of a coarse detrital component with low  $^9\text{Be}$  and very low  $^{10}\text{Be}$ ;

- from 0.54 mbsf to the top of the sediment core, the initial  $^{10}\text{Be}/^9\text{Be}$  ratio continued to decrease to a value of ca.  $0.28 \times 10^{-7}$ , but in a non-systematic way. Uptake of beryllium by the sediment was extremely variable due, probably, to rapidly changing composition of the detritus in conditions of very low net sedimentation.

A plot of initial  $^{10}\text{Be}/^9\text{Be}$  vs. the inverse of  $^9\text{Be}$  concentration (Fig. 8) illustrates the three phases outlined above. The negative linear correlation from 3.54 to 1.04 mbsf is indicative of binary mixing between a high  $^{10}\text{Be}/^9\text{Be}$ , high  $^9\text{Be}$  end-member (seawater) and a low  $^{10}\text{Be}/^9\text{Be}$ , low  $^9\text{Be}$  end-member (coarse detrital component). Below 0.54 mbsf, a positive, but poor correlation results from either the introduction of additional components in the mix, or variable extraction of beryl-

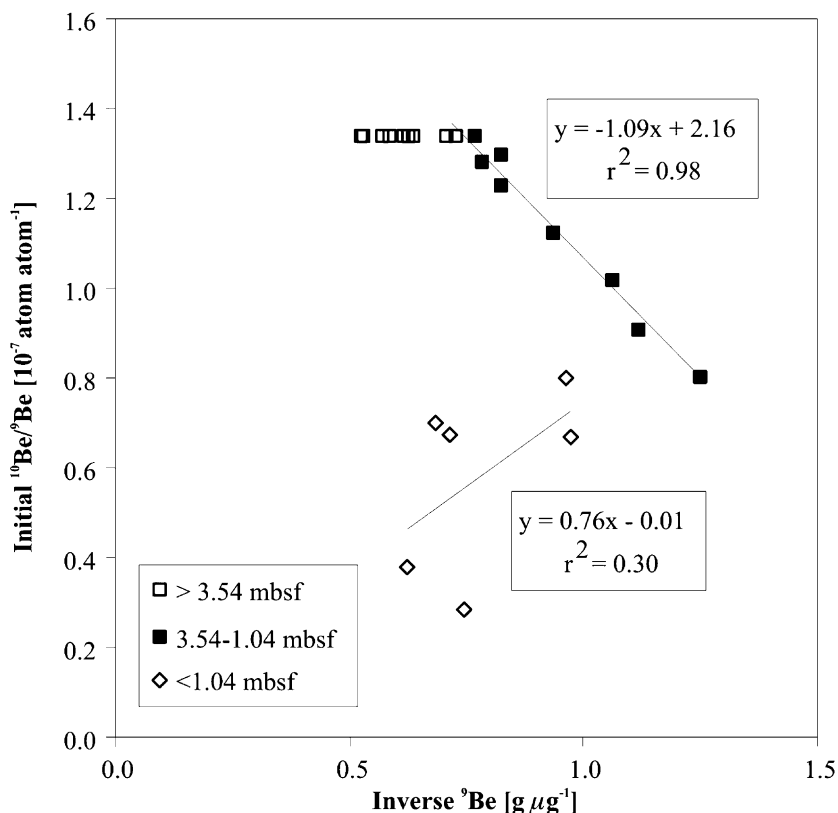


Fig. 8. Initial  $^{10}\text{Be}/^9\text{Be}$  vs. inverse  $^9\text{Be}$  concentration for Site 1121 sediments.

lium. These divisions are consistent with observed changes in sediment grain-size at 4.16–3.86 mbsf and 0.73–0.44 mbsf (Table 1). Because of the lack of entrapped nodules below ca. 4 mbsf, it is difficult to interpret the observed variation in  $^{10}\text{Be}/^9\text{Be}$  ratios (Figs. 3 and 4), in particular the apparent age reversals (Table 5, Model 1). Hence, it is deemed better to calculate the age of the sediment core below 4 mbsf by simply applying the sedimentation rate to 4.08 mbsf of  $39.2 \text{ cm m.y.}^{-1}$  (i.e. Model 2, Table 5).

#### 5.4. Flux rates

$^{10}\text{Be}$  concentrations in the sediment to 7.04 mbsf, corrected for radioactive decay using Model 2, range from  $2.6$  to  $41.2 \times 10^9 \text{ atoms g}^{-1}$ , averaging  $12 \times 10^9 \text{ atoms g}^{-1}$ . This translates into a

mean  $^{10}\text{Be}$  flux rate (i.e. sedimentation rate  $\times$  dry bulk density  $\times$  mean  $^{10}\text{Be}$  concentration) of  $3.5 \times 10^5 \text{ atoms cm}^{-2} \text{ y}^{-1}$ . This value is similar to other open ocean sediment cores (e.g.  $5 \times 10^5 \text{ atoms cm}^{-2} \text{ y}^{-1}$  – DSDP Site 519, Henken-Melies et al., 1990;  $7 \times 10^5 \text{ atoms cm}^{-2} \text{ y}^{-1}$  – North Atlantic, Southon et al., 1987), despite the more than one order of magnitude lower sedimentation rate at Site 1121. The derived flux of  $3.5 \times 10^5 \text{ atoms cm}^{-2} \text{ y}^{-1}$  is a factor of 3.4 lower than the estimate of the global average  $^{10}\text{Be}$  production rate of Monaghan et al. (1985/86). This is not surprising given the much higher flux rates into ocean margin sediments (Anderson et al., 1990; Frank et al., 1995), which results in depletion at open ocean sites. The  $^{10}\text{Be}$  flux into the Site 1121 sediment shows a rapid decline from ca.  $5.0$  to  $1.5 \times 10^4 \text{ atoms cm}^{-2} \text{ y}^{-1}$ , beginning at ca.

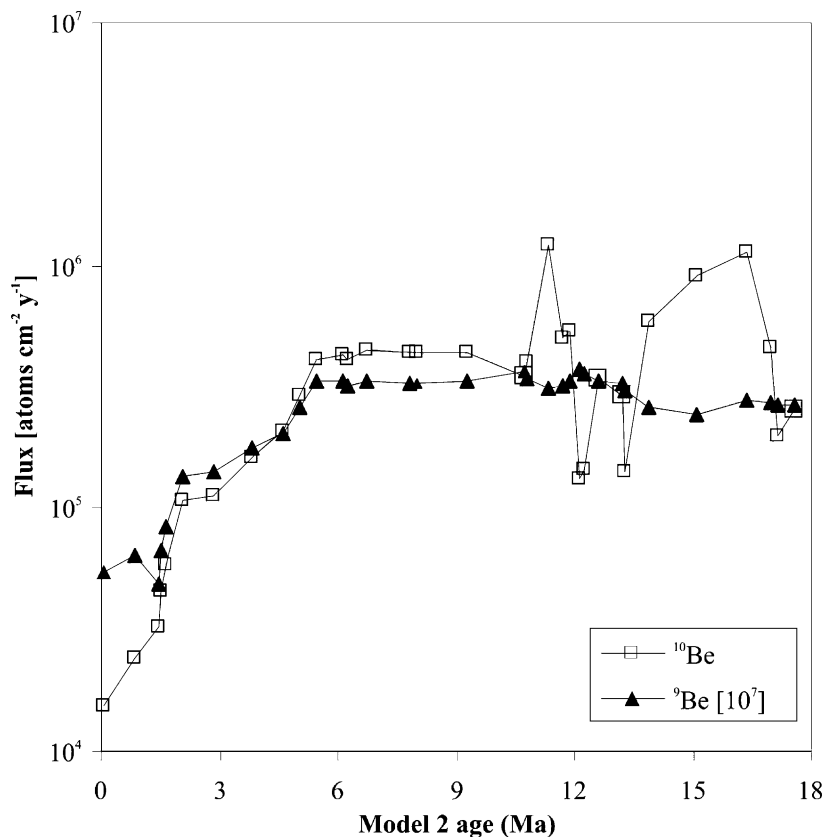


Fig. 9. Beryllium isotope flux vs. age for Site 1121 sediments. Flux calculations use measured concentrations, Model 2 ages, and dry densities extrapolated from measured values: 7.33 (1.12–1.18 mbsf), 7.24 (5.56 mbsf), 7.56 (8.86 mbsf).

3 mbsf (Fig. 9). This pattern is due to rapidly falling  $^{10}\text{Be}$  concentrations towards the top of the sediment core rather than to changes in sedimentation rate (there is a similar result if a constant sedimentation rate of  $39\text{ cm m.y.}^{-1}$  is applied).  $^9\text{Be}$  flux rate decreases in a similar way to  $^{10}\text{Be}$ , although there is a de-coupling near the top of the sediment core. Overall, the observed changes in flux rate are consistent with changes in sediment characteristics, in particular the gradual increase in coarse detritus with relatively low beryllium content and low  $^{10}\text{Be}/^9\text{Be}$  ratio towards the top of the core.

## 6. Stratigraphic and palaeo-oceanographic interpretation

The modelled  $^{10}\text{Be}/^9\text{Be}$  data provide evidence for a relatively coherent chronostratigraphy for the sediment core from ca. 4 mbsf to the top (Fig. 7). Below ca. 4 mbsf, the dating becomes increasingly less precise so that, by ca. 7 mbsf, errors are more than  $\pm 12\%$ , and by ca. 8.5 mbsf they exceed  $\pm 30\%$ . This, in part, explains the irregular dating results, including reversals, in the lower part of the core (Table 5, Model 1). However, the coherency of adjacent  $^{10}\text{Be}/^9\text{Be}$  ratios indicates that some of this variability relates to compositional changes (e.g. influx of phosphate at ca. 5.5 mbsf) and, possibly, bioturbation. (But note that the  $^{10}\text{Be}/^9\text{Be}$  age pattern is not unduly disturbed where bioturbation appears to be most intense; Fig. 4.)

From preliminary microfossil analysis, Carter et al. (1999, p. 19) concluded that the upper 3 m of sediment at Site 1121 represents a condensed sequence of Plio–Pleistocene age, underlain by 2 m of early Late Pliocene sediment and a further 27 m of unspecified late Neogene material. The Model 2  $^{10}\text{Be}/^9\text{Be}$  age for ca. 1 mbsf, 2.8 Ma, is consistent with a diatom biostratigraphic age of 2.2–3.6 Ma. Also, a projection of the overall sedimentation rate of  $39\text{ cm m.y.}^{-1}$  (Table 7) to 15.2 mbsf (the Unit 1A/1B boundary) yields an age of 39 Ma for the unconformity between the Neogene ‘skin-drift’ (Unit 1A) and the underlying Palaeocene chalk and chert (Unit 1B, which is well dated to

57.5–61.0 Ma based upon detailed radiolarian biostratigraphy; Hollis, 2002). The hiatus between ca. 39 and 59 Ma at Site 1119 (Fig. 1) results from seafloor erosion along the regional Marshall Paraconformity, which marks the flow of vigorous, cold bottom waters of southern origin caused by Eocene–Oligocene climatic deterioration. We note that even a slightly lower sedimentation rate over the lower part of the ‘skin-drift’ succession would suffice to bring our 39 Ma estimate for the age of its base into line with the known ca. 33 Ma age of the paraconformity at other localities (cf. Fulthorpe et al., 1996). Overall, from our analysis, it is clear that  $^{10}\text{Be}/^9\text{Be}$  dating, even taking account of the uncertainties and assumptions associated with it, is able to improve significantly on those preliminary biostratigraphic interpretations.

Above ca. 4 mbsf, calculated sedimentation rates vary significantly: from ca.  $19\text{ cm m.y.}^{-1}$  at 4.1–3.2 mbsf; ca.  $95\text{ cm m.y.}^{-1}$  at 3.2–1.4 mbsf; ca.  $58\text{ cm m.y.}^{-1}$  at 1.4–0.1 mbsf; to ca.  $8\text{ cm m.y.}^{-1}$  at 0.1–0 mbsf (Table 7). Apart from the occurrence of the very small nodule at 1.43 mbsf, the two slower periods of sedimentation coincide with the appearance of entrapped nodules, possibly indicating enhanced conditions for nodule formation in the vicinity of Site 1121 at those times. (We note that sediment samples analysed between 3.18 and 0.12 mbsf failed to produce chlorine gas during leaching, confirming the absence of ferromanganese fragments in the sediment, and indicating that the nodule at 1.43 mbsf was a rare and isolated occurrence.) The overall sedimentation rate of ca.  $39\text{ cm m.y.}^{-1}$  whilst slow, is not unreasonable given that Site 1121 is at 4503 m water depth where significant solution of biopelagic carbonate has occurred. (At DSDP site 519 in the central South Atlantic, the overall sedimentation rate is ca.  $1350\text{ cm m.y.}^{-1}$ , Henken-Mellies et al., 1990, which, given a carbonate content of 90%, implies a non-carbonate sedimentation rate of ca.  $135\text{ cm m.y.}^{-1}$ .)

The dating results, then, indicate pulses of faster and slower sedimentation, with the slower sedimentation representing times during which the Campbell Nodule Field and its environs was subjected to more vigorous DWBC circulation. At such times, the finer sediment particles were win-

nosed out, and nodule growth encouraged both by the lack of accumulating sediment and by the constant recharge of Fe–Mn-rich bottom water and consequent biogenic activity. Thus we infer strong DWBC activity at Site 1121 during the late Miocene at ca. 10–5.5 Ma. The initiation of the Campbell Nodule Field, as suggested by the age of the largest recovered seafloor nodule ( $14.9 \pm 0.4$  Ma; Graham et al., 2003) relates approximately to the end of phosphatisation. The Campbell Nodule Field began during a phase of increasing DWBC activity between ca. 15.5 and 12.5 Ma, inferred by Hall et al. (2003) from grain-size analysis, and also during the well known middle Miocene cooling phase CM4 (Woodruff and Savin, 1991; Flower and Kennett, 1995), which is believed to represent marked climatic deterioration and the development of the East Antarctic ice-sheet (e.g. Zachos et al., 2001).

The continued presence of the widespread Campbell Nodule Field and the appearance of nodules at shallow depths in the Site 1121 sediment core is consistent with DWBC activity throughout the Plio–Pleistocene, especially during glacial periods (cf. Hall et al., 2001, 2002). Punctuated biostratigraphic hiatuses over this time period, which may indicate phases of vigorous current flow, have been inferred at nearby shallow water Site 1120 on the Campbell Plateau (Fig. 1) (Carter et al., 1999). However, more detailed work is required to determine the precise age of the 1120 hiatuses, and to correlate these with results from Site 1121.

## 7. Summary and conclusions

Beryllium isotopic analysis of the ODP 181 Site 1121 sediment core has yielded new information about its character and stratigraphy:

- Entrapped ferromanganese nodules, of hydrogenous origin, occur at various depths in the sediment core to 4.08 mbsf. The nodules have similar chemistry and growth rates to seafloor nodules of the Campbell Nodule Field, from where they originated. Their core and rim ages, based on initial  $^{10}\text{Be}/^9\text{Be}$  ratios equal to contemporary seawater, decrease with depth in the sediment core, the rim

ages providing the basis for a chronostratigraphy to ca. 4 mbsf.

- Measured  $^{10}\text{Be}/^9\text{Be}$  ratios of the core sediment to ca. 7 mbsf provide a complementary chronology to that of the entrapped nodules. From ca. 4.1–3.2 mbsf, the sediment ages and nodule rim ages broadly agree. Above this, increasing influence of coarse silicate detritus with relatively low  $^{10}\text{Be}/^9\text{Be}$  results in the sediment yielding progressively higher ages than the associated nodules until, at the surface, the difference is 3.4 m.y.

- Based on a model combining the sediment and the entrapped nodule data, the sediment core to a depth of ca. 7 mbsf has an age of 17.6 Ma, corresponding to an overall sedimentation rate of ca.  $39 \text{ cm m.y.}^{-1}$ . Slower periods of sedimentation are marked by the appearance of buried nodules at ca. 10–5.5 Ma and ca. 1.5–0 Ma, reflecting enhanced formation conditions in the Campbell Nodule Field due to increased DWBC activity.

- The study indicates that deep-sea sediments can be dated with  $^{10}\text{Be}/^9\text{Be}$ , producing useful and unexpected results, but this must be accompanied by independent age indicators for absolute calibration (e.g. entrapped ferromanganese nodules).

## References

- Anderson, R.F., Lao, Y., Broecker, W.S., Trumbore, S.E., Hofmann, H.J., Wolff, W., 1990. Boundary scavenging in the Pacific Ocean: A comparison of  $^{10}\text{Be}$  and  $^{231}\text{Pa}$ . *Earth Planet. Sci. Lett.* 96, 287–304.
- Baturin, G.N., Savenko, V.S., 1989. Growth rates of deep-water iron-manganese nodules. *Oceanology* 29, 334–342.
- Bhat, S.G., Krishnaswamy, S., Lal, D., Somayajulu, B.L.K., 1973. Radiometric and trace element studies of ferromanganese nodules. In: *Symposium on Hydrochemistry and Biogeochemistry, VI, Hydrogeochemistry*, 443–462.
- Bourlès, D., Raisbeck, G.M., Yiou, F., 1989.  $^{10}\text{Be}$  and  $^9\text{Be}$  in marine sediments and their potential for dating. *Geochim. Cosmochim. Acta* 53, 443–452.
- Carter, L., McCave, I.N., 1997. The sedimentary regime beneath the Deep Western Boundary Current inflow to the SW Pacific Ocean. *J. Sediment. Res.* 67, 1005–1017.
- Carter, R.M., McCave, I.N., Richter, C.A., Carter, L., et al., 1999. ODP Initial Reports 181, Ocean Drilling Program, Texas A&M University, College Station, TX 77845–9547 [CD-ROM] ([http://www-odp.tamu.edu/publications/181\\_IR/chap\\_05.htm](http://www-odp.tamu.edu/publications/181_IR/chap_05.htm)).

- Ditchburn, R.G., Graham, I.J., 2003. Preparation Procedures for the  $^{10}\text{Be}$  Analysis of Marine Deposits. GNS Science Report 2003/10, 24 pp.
- Flower, B.P., Kennett, J.P., 1995. Middle Miocene deep water paleoceanography in the southwest Pacific: Relations with East Antarctic Ice Sheet development. *Paleoceanography* 10, 1095–1112.
- Frank, M., Eisenhauer, A., Bonn, W.J., Walter, P., Grobe, H., Kubik, P.W., Ditttrich-Hannen, B., Mangini, A., 1995. Sediment redistribution versus productivity change: Weddell Sea Margin sediment stratigraphy and biogenic particle flux of the last 250,000 years deduced from  $^{230}\text{Th}_{\text{ex}}$ ,  $^{10}\text{Be}$  and biogenic barium profiles. *Earth Planet. Sci. Lett.* 136, 559–573.
- Fulthorpe, C.S., Carter, R.M., Miller, K.G., Wilson, J., 1996. The Marshall Paraconformity: A Southern Hemisphere record of a mid-Oligocene glacioeustatic lowstand? *Mar. Pet. Geol.* 13, 61–77.
- Graham, I.J., Ditchburn, R.G., Zondervan, A., Chang, S.W., Choi, H., Lee, S.R., Wright, I.C., 2003. Ferromanganese nodules in the vicinity of Bollons Seamount SE of the Campbell Plateau, SW Pacific Ocean. Part 3: Beryllium isotope dating. GNS Science Report 2003/15, 40 pp.
- Hall, I.R., McCave, I.N., Shackleton, N.J., Weedon, G.P., Harris, S.E., 2001. Intensified deep Pacific inflow and ventilation in Pleistocene glacial times. *Nature* 412, 809–812.
- Hall, I.R., Carter, L., Harris, S.E., 2002. Major depositional events under the deep Pacific inflow. *Geology* 30, 487–490.
- Hall, I.R., McCave, I.N., Zahn, N., Carter, L., Knutz, C.P., Weedon, G.P., 2003. Paleocurrent reconstruction of the deep Pacific inflow during the middle Miocene: Reflections of East Antarctic Ice Sheet growth. *Paleoceanography* 18; doi:10.1029/2002PA000817.
- Henken-Mellies, W.U., Beer, J., Heller, F., Hsü, K.J., Shen, C., Bonani, G., Hofmann, H.J., Suter, M., Wöfl, W., 1990.  $^{10}\text{Be}$  and  $^9\text{Be}$  in South Atlantic DSDP Site 519: Relation to geomagnetic reversals and to sediment composition. *Earth Planet. Sci. Lett.* 98, 267–276.
- Hollis, C.J., 2002. Biostratigraphy and paleoceanographic significance of Paleocene radiolarians from offshore eastern New Zealand. *Micropaleontology* 887, 1–52.
- Janin, M.-C., 1987. Micropaleontology of manganese nodules from the equatorial North Pacific Ocean – area SO 25-1 and SO 25-3. In: von Stackelberg, U., Beiersdorf, H. (Eds.), *Manganese Nodules and Sediments in the Equatorial North Pacific Ocean*. *Geol. Jhrb.* D87, 315–376.
- Kennett, J.P., Houtz, R.E., Andrews, P.B., Edwards, A.R., Gostin, V.A., Hajos, M., Hampton, M., Jenkins, G.D., Margolis, S.V., Ovenshine, A.T., Perch-Neilson, K., 1973. Deep-drilling in the roaring 40s. *Geotimes*, 14–17.
- Kusakabe, M., Ku, T.-L., 1984. Incorporation of beryllium isotopes and other trace metals into marine ferromanganese deposits. *Geochim. Cosmochim. Acta* 48, 2187–2193.
- Kusakabe, M., Ku, T.-L., Southon, J.R., Vogel, J.S., Nelson, D.E., Measures, C.I., Nozaki, Y., 1987. The distribution of  $^{10}\text{Be}$  and  $^9\text{Be}$  in ocean water. *Nucl. Instr. Meth. Phys. Res. B* 29, 306–310.
- Li, Y.H., 1982. Inter-element relationship in abyssal Pacific ferromanganese nodules and associated pelagic sediments. *Geochim. Cosmochim. Acta* 46, 1053–1060.
- Li, Y.H., 1991. Distribution patterns of the elements in the ocean: A synthesis. *Geochim. Cosmochim. Acta* 55, 3223–3240.
- Ling, H.F., Burton, K.W., O’Nions, R.K., Kaluber, B.S., von Blanckenburg, F., Gibbs, A.J., Hein, J.R., 1997. Evolution of Nd and Pb isotopes in Central Pacific seawater from ferromanganese crusts. *Earth Planet. Sci. Lett.* 146, 1–12.
- Mangini, A., Segl, M., Kudrass, H., Wiedicke, M., Bonani, G., Hofmann, J., Morenzoni, E., Nessi, M., Suter, M., Wöfl, W., 1986. Diffusion and supply rates of  $^{10}\text{Be}$  and  $^{230}\text{Th}$  radioisotopes in two manganese encrustations from the South China Sea. *Geochim. Cosmochim. Acta* 50, 149–156.
- Mangini, A., Segl, M., Glasby, G.P., Stoffers, P., Plüger, W.L., 1990. Element accumulation rates and growth histories of manganese nodules from the Southwestern Pacific Basin. *Mar. Geol.* 94, 97–107.
- McHargue, L.R., Damon, P.E., 1991. The global beryllium 10 cycle. *Rev. Geophys.* 29, 141–158.
- Middleton, R., Brown, L., Dezfouly-Arjomandy, B., Klein, J., 1993. On  $^{10}\text{Be}$  standards and the half-life of  $^{10}\text{Be}$ . *Nucl. Instr. Meth. B* 82, 399–403.
- Monaghan, M.C., Krishnaswami, S., Turekian, K.K., 1985. The global-average production rate of  $^{10}\text{Be}$ . *Earth Planet. Sci. Lett.* 76, 279–287.
- Nishiizumi, K., 2002.  $^{10}\text{Be}$ ,  $^{26}\text{Al}$ ,  $^{36}\text{Cl}$ , and  $^{40}\text{Ca}$  standards. Abstracts, Ninth International Conference on Accelerator Mass Spectrometry, Nagoya, September 9–13, 2002.
- Segl, M.A., Mangini, A., Beer, J., Bonani, G., Suter, M., Wöfl, W., 1984.  $^{10}\text{Be}$  dating of a manganese crust from Central North Pacific and implications for oceanic paleocirculation. *Nature* 309, 540–543.
- Segl, M.A., Mangini, A., Beer, J., Bonani, G., Suter, M., Wöfl, W., 1989. Growth rate variations of manganese nodules and crusts induced by paleoceanographic events. *Paleoceanography* 4, 511–530.
- Somayajulu, B.L.K., 2000. Growth rates of oceanic manganese nodules: Implications to their genesis, palaeo-earth environment and resource potential. *Curr. Sci.* 78, 300–308.
- Southon, J.R., Ku, T.L., Nelson, D.E., Reys, J.L., Duplessy, J.C., Vogel, J.S., 1987.  $^{10}\text{Be}$  in a deep-sea core: Implications regarding  $^{10}\text{Be}$  production changes over the past 420 ka. *Earth Planet. Sci. Lett.* 85, 356–364.
- von Blanckenburg, F., Igel, H., 1999. Lateral mixing and advection of reactive isotope tracers in ocean basins: Observations and mechanisms. *Earth Planet. Sci. Lett.* 169, 113–128.
- von Blanckenburg, F., O’Nions, R.K., 1999. Response of beryllium and radiogenic isotope ratios in Northern Atlantic Deep water to the onset of northern hemisphere glaciation. *Earth Planet. Sci. Lett.* 167, 175–182.
- von Blanckenburg, F., O’Nions, R.K., Belshaw, N.S., Gibb, A., Hein, J.R., 1996. Global distribution of beryllium isotopes in deep ocean water as derived from Fe–Mn crusts. *Earth Planet. Sci. Lett.* 141, 213–226.
- von Stackelberg, U., 1984. Significance of benthic organisms

- for the growth and movement of manganese nodules, Equatorial North Pacific. *Geo-Mar. Lett.* 4, 37–42.
- von Stackelberg, U., 1987. Pumice and buried manganese nodules from the equatorial North Pacific Ocean. In: von Stackelberg, U., Beiersdorf, H. (Eds.), *Manganese nodules and sediments in the Equatorial North Pacific Ocean*. *Geol. Jahrb.* D87, 229–286.
- von Stackelberg, U., 1997. Growth history of manganese nodules and crusts in the Peru Basin. In: Nicholson, K., Hein, J.R., Buhn, B., Dasgupta, S. (Eds.), *Manganese mineralisation: Geochemistry and mineralogy of terrestrial and marine deposits*. *Geol. Soc. London Spec. Publ.* 119, 153–176.
- von Stackelberg, U., Marchig, V., 1987. Manganese nodules from the equatorial North Pacific Ocean. In: von Stackelberg, U., Beiersdorf, H. (Eds.), *Manganese nodules and sediments in the Equatorial North Pacific Ocean*. *Geol. Jhb.* D87, 123–228.
- Walcott, R.I., 1998. Modes of oblique compression: Late Cenozoic tectonics of the South Island of New Zealand. *Rev. Geophys.* 36, 1–26.
- Weber, M.E., von Stackelberg, U., Marchig, V., Wiedicke, M., Grupe, B., 2000. Variability of surface sediments in the Peru Basin: Dependence on water depth, productivity, bottom water flow, and sea floor topography. *Mar. Geol.* 163, 169–184.
- Wentworth, C.K., 1922. A scale of grade class terms for clastic sediments. *J. Geol.* 300, 377–392.
- Woodruff, F., Savin, S., 1991. Mid-Miocene isotope stratigraphy in the deep sea: High resolution correlations, paleoclimatic cycles, and sediment preservation. *Paleoceanography* 6, 755–806.
- Wright, I.C., Graham, I.J., Chang, S.W., Choi, H., Lee, S.R., 2003. Occurrence and physical setting of ferromanganese nodules beneath the Deep Western Boundary Current – eastern Campbell Plateau Sector, SW Pacific. *N.Z.J. Geol. Geophys.* (submitted).
- Zachos, J., Pagani, M., Sloan, L., Thomas, E., Billups, K., 2001. Trends, rhythms, and aberrations in global climate 65 Ma to present. *Science* 292, 686–693.
- Zondervan, A., 2001. Be-10 and Al-26 AMS Capability at GNS: Status 2001. *GNS Science Report* 2001/15.